Proceedings of the 29th Annual Conference of the Computational Fluid Dynamics Society of Canada
CFDSC2021
July 27-29, 2021, Online

Non-equilibrium turbulent boundary layer with adverse pressure gradient and convex wall curvature

Saurabh Pargal[1,2], Hao Wu[2], Junlin Yuan[1] and Stéphane Moreau[2]

[1] *Department of Mechanical Engineering, Michigan State University, East Lansing, Michigan, USA*
[2] *Department of Mechanical Engineering, Université de Sherbrooke, Sherbrooke, Québec, Canada*

Email: *pargalsa@msu.edu*

Abstract

Direct numerical simulations (DNS) of flows over an airfoil (suction side) and a flat plate are compared to characterize non-equilibrium turbulent boundary layers with wall curvature. The two simulations have matched adverse pressure gradient (APG) quantified by the acceleration parameter (K). For the airfoil flow, an existing DNS carried out by Wu et al. [1] of the flow around a controlled-diffusion (CD) airfoil is used. For the flat-plate flow, a separate simulation is carried out to match the K distribution in the APG region of the airfoil boundary layer flow and data collection for flow/acoustic model development. The difference between the two cases represents the effect of a mild convex wall curvature. Specifically, in the region of weak APG, the curvature effect dominates that of the pressure gradient and yields a lower friction coefficient. In the high-APG region (near the trailing edge of the airfoil) the effects of wall curvature and APG appear to interact. Overall, the comparison between the two flows shows that the boundary layer developments are very similar. This indicates that a flat-plate boundary layer can serve as a low-cost surrogate of an airfoil boundary layer in numerical studies of important features of an airfoil flow.

1 INTRODUCTION

Turbulent boundary layer flows are ubiquitous. Current understanding of flow physics and existing turbulence closures are usually focused on equilibrium (self-similar) flows. Yet, most flows encountered in realistic applications such as ventilation systems are non-equilibrium flows characterized by unsteadiness, pressure gradients, and wall curvature. Existing turbulence models often yield large uncertainties in non-equilibrium flows. One example is shown by Yuan et al. [2] for flows with strong pressure gradients.

This work focuses on a subset of non-equilibrium turbulent flows—those with streamwise adverse pressure gradient and convex wall curvature. This type of flow is widely found in industrial applications, from heating, ventilation and cooling (HVAC) system to cooling fans in computers, from cars to airplanes, and from turbines in hydro-power plants to household water pumps. Typically, the pressure gradient experienced by the boundary layer is generated by the wall curvature. The strength of a pressure gradient can be quantified by the the Clauser parameter $\beta = (\delta^*/\tau_w)(dp/dx)$, where δ^* is the displacement thickness, τ_w is the wall-shear stress, dp/dx is the local streamwise gradient of the mean pressure and x is streamwise direction. For a non-equilibrium boundary layer subjected to pressure gradients, β is not constant. In this case, the flow depends on not only the local magnitude of β, but also its streamwise variation. This non-local dependence is called "history effect" [3]. The APG effects on a boundary layer include a faster increase in boundary layer thickness and decrease in skin friction. Also, the Reynolds stresses are increased in the outer region, but reduced near the wall, suggesting that the turbulence in the outer region are energized.

Most existing studies aimed to understand the sensitivity of boundary layers to longitudinal convex curvatures, keeping pressure gradient minimal to separate the two effects. For example, Bradshaw [4] showed that a boundary layer thickness (δ) as small as 1/300 times that of the radius of curvature (R) has an effect on turbulence length scales in the boundary layer. So and Mellor [4] found that, for relatively high convex curvatures ($\delta/R > 0.1$), the Reynolds stress decrease near the wall, and even more so in the outer layer.

The objective of this work is to understand the effect of convex curvature in the presence of APG that is relevant to fan applications. To this end, DNS simulations of flow over a CD airfoil and flow over a flat plate are compared. Both flows are subjected to matching streamwise pressure gradient quantified by the acceleration parameter, $K = (\nu/U_\infty^2)(dU_\infty/dx)$, where ν is the kinematic viscosity, and U_∞ is the streamwise freestream velocity. Comparison between the two cases isolates the effect of wall curvature, which is characterized in this work.

2 Approach

Data of the CD airfoil flow are available from Wu et al [1]. The distribution of $K(x)$ of the boundary layer on the suction side is shown in Fig. 1(a). A separate DNS of a flat-plate boundary layer is conducted. It is designed to match the $K(x)$ distribution of the airfoil flow in the APG region only (i.e. from around mid-chord, $x/c = -0.6$, to the trailing edge, where c is the airfoil chord length). The equivalent airfoil $x/c = -0.6$ location corresponding to the start of flat plate simulation as denoted as x_0.

The incompressible flow of a Newtonian fluid is governed by the equations of conservation of mass and momentum:

$$\frac{\partial u_i}{\partial x_i} = 0, \tag{1}$$

$$\frac{\partial u_j}{\partial t} + \frac{\partial u_i u_j}{\partial x_i} = -\frac{\partial P}{\partial x_j} + \nu \nabla^2 u_j \tag{2}$$

Here, x_1, x_2 and x_3 (or x, y and z) are, respectively, the streamwise, wall-normal and spanwise directions, and u_j (or u, v and w) are the velocity components in those directions. Here t is time, $P = p/\rho$ is the modified pressure, ρ is the density and ν is the kinematic viscosity. The flat-plate simulation is performed using a well-validated code that solves the governing equations (1) and (2) on a staggered grid using second-order, central differences for all spatial derivatives, second-order accurate Adams-Bashforth semi-implicit time advancement, and MPI parallelization [10]. An instantaneous flow variable $\theta(x,y,z,t)$ can be decomposed as $\theta = \langle\overline{\theta}\rangle(x,y) + \theta'(x,y,z,t)$, where $\langle\cdot\rangle$ denotes spatial averaging in z and $\overline{(\cdot)}$ denotes averaging in time.

For the flat-plate boundary layer, the pressure gradient is imposed by prescribing the streamwise-varying $U_\infty(x)$ at the top boundary of the domain (shown in Figure 1(b)); the wall-normal freestream velocity V_∞ is obtained based on the conservation of mass. A fully turbulent boundary layer flow at the inlet is obtained using the recycling/rescaling method. A convective outflow boundary condition is used at the outlet and periodic boundary conditions are used in the spanwise direction.

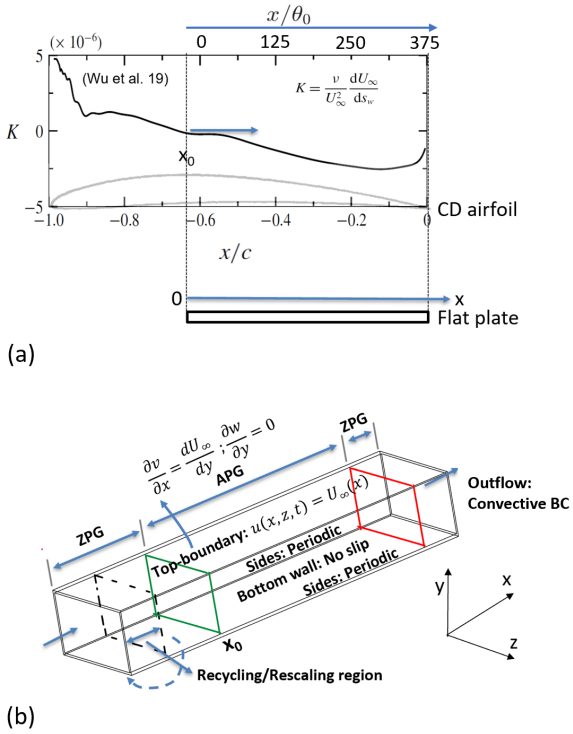

Figure 1: (a) Sketch of the streamwise simulation domain of the flat-plate flow designed to match $K(x)$ of the CD airfoil boundary layer from x_0 onward. (b) Domain and boundary conditions used in the flat-plate flow DNS.

Uniform grids are used in x and z, while in y the grids are stretched such that the spatial resolution is finer near the wall. At the x_0 location, $\Delta x^+ = 10$, $\Delta z^+ = 5$ and $\Delta y^+_{min} = 0.15$. The total number of grid points are $1536 \times 200 \times 256$ in x, y and z directions.

A well-validated in-house code is used to solve the continuity and momentum equations of an incompressible fluid. The solver is based on a staggered mesh and is second-order accurate in both time and space. The Reynolds numbers based on the momentum thickness (θ_0) at the x_0 are both 320 in the two cases.

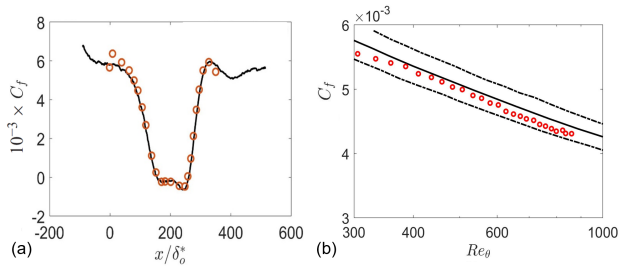

Figure 2: Skin friction comparison of (a) present test case (black line) with Na and Moin [8] (symbols) and (b) present test case (red symbols) with DNS data shown by Schlatter and Örlü [7] (black line with dash dotted lines indicating 5 percent tolerance)

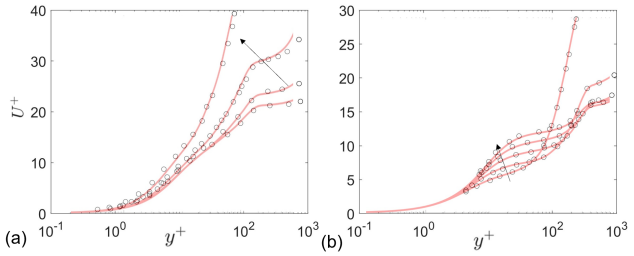

Figure 3: Validation of streamwise mean velocity with Na and Moin [8] (circles): (a) before detachment ($x/\delta^* = 100$, 115, 130, 145 in arrow direction) and (b) after reattachment ($x/\delta^* = 270$, 285, 300, 330 in arrow direction).

The fluid solver is validated by running a zero-pressure gradient (ZPG) flat-plate boundary layer simulation and comparing with the results of Schlatter and Örlü [7]. The C_f comparison is shown in Figure 2(b); excellent agreement is shown. To validate the prescription of the mean adverse pressure gradient, another DNS is carried out to reproduce the results of a separating APG boundary-layer flow conducted by Na and Moin [8]. Very good agreement in C_f is shown in Figure 2(a), and the agreements in the mean velocity ($U \equiv \langle \overline{u} \rangle$) profiles before and after the boundary layer separation are shown in Figure 3.

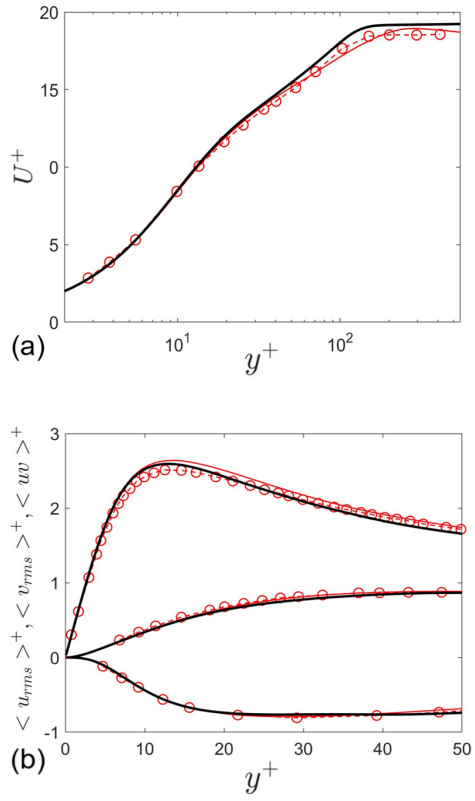

Figure 4: Inlet comparison between the airfoil (red solid line) and flat-plate cases (black solid line): (a) streamwise mean velocity and (b) Reynolds stresses normalized by inner units Red circles: Spalart [9].

3 Results

3.1 Statistics at the inlet of flat-plate boundary layer

From here on, the x_0 location at the airfoil is set as $x = 0$ (and called the "inlet") for the flat-plate simulation. A prerequisite of the comparison between the developments of the airfoil and the flat-plate boundary layers is that the flat-plate flow at the inlet matches the airfoil flow at the corresponding location ($x/c = -0.6$). In Figure 4, the comparison between the streamwise mean velocity and the Reynolds stresses are shown, together with the results of a ZPG boundary layer simulation by Spalart [7] at a similar Reynolds number of $Re_\theta = 300$. The profiles of all cases match very well overall. The mean velocity profile in the flat-plate simulation is slightly higher in the outer region, which is probably due to the adverse pressure gradients imposed downstream. Moreover, the streamwise fluctuations for the airfoil case is around 5 percent higher than the results of Spalart [7] for $y^+ > 10$, which is probably due to the favorable pressure gradient upstream of this location as a result of the curvature.

Two-point correlations of u' and v' are compared in Figures 5 to 7, in various planes. Results of Sillero et al. [9] is also compared. Sillero et al. [9] calculated two-point velocity statistics from a DNS simulation of a ZPG turbulent boundary layer, with Reynolds numbers of $Re_\theta = 2780 - 6680$. Although this Reynolds number is an order of magnitude higher than that in the present simulations, the qualitative features of two-point correlations are insensitive to the Reynolds number as shown in by Sillero et al. [9].

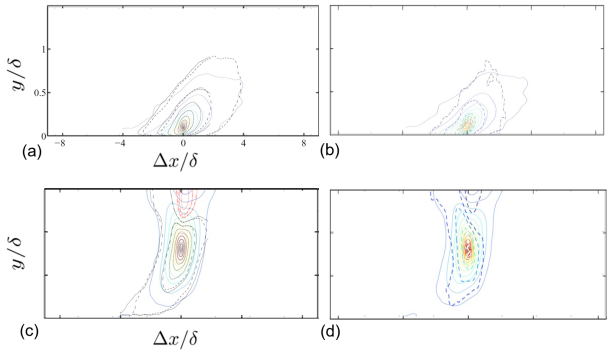

Figure 5: Inlet comparison of two-point autocorrelations of u' in $x-y$ plane at y/δ=0.1 (a,b) and y/δ=0.8 (c,d). In (a,c), the airfoil case (blue contour is low value and red contour is high value) and Sillero et al. [9] (black is positive and red is negative value) are compared. In (b,d), airfoil and flat-plate (coloured dashed contours) cases are compared. Contour level are from 0.05 to 0.6 with a step size of 0.05.

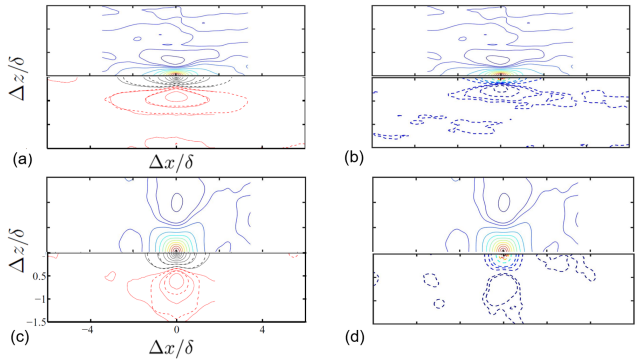

Figure 6: Inlet comparison of two-point autocorrelations of u' in $x-z$ plane at $y/\delta = 0.1$ (a,b) and $y/\delta = 0.8$ (c,d). In (a,c), the airfoil case (top, blue is low value and red is high value) and Sillero et al. [9] (bottom, black is positive value and red is negative value) are compared. In (b,d), the airfoil (top) and flat-plate (bottom, coloured dashed contours) cases are compared. Contour levels are from 0.05 to 0.6 with a step size of 0.05.

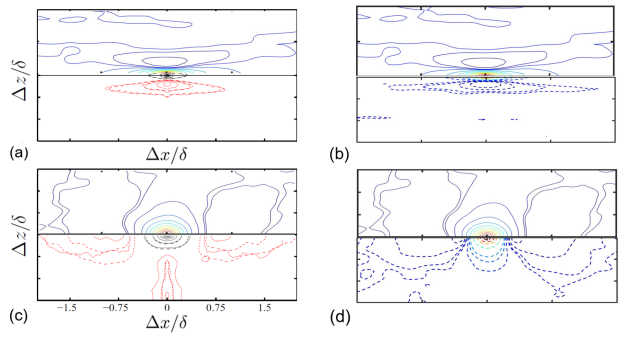

Figure 7: Inlet comparison of two-point autocorrelations of v' in $x-z$ plane at $y/\delta = 0.1$ (a,b) and $y/\delta = 0.8$ (c,d). In (a,c), the airfoil case (top, blue is low value and red is high value) and Sillero et al. [9] (bottom, black is positive value and red is negative value) are compared. In (b,d), airfoil (top) and flat-plate (bottom, coloured dashed contours) cases are compared. Contour levels are from 0.05 to 0.6 with a step size of 0.05.

Figure 5(a,b) and (c,d) show the two-point autocorrelations of u' in the $x-y$ plane at two wall-normal locations: $y/\delta = 0.1$ and $y/\delta = 0.8$. At the near-wall elevation, the inclined iso-contours show the inclination of velocity streaks. At the higher elevation, the correlations indicate tall and large coherent motions, spanning the whole boundary layer thickness. The overall shapes of the two-point correlation compare well among all cases. In Figure 6, two-point autocorrelations of u' in the $x-z$ plane are shown, again at the two different elevations. One observes a spanwise symmetry due to the homogeneity of the flow in the spanwise direction. The contour lines show alternating streamwise streaks along the spanwise direction, a feature shown in all cases.

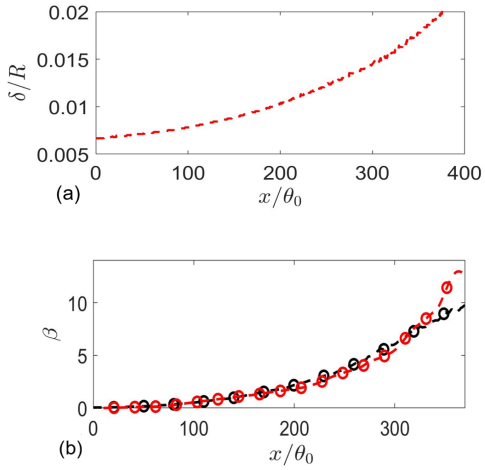

Figure 8: Comparisons of (a) ratio between boundary layer thickness and the radius of curvature of airfoil and (b) Clauser parameter between the airfoil (red) and the flat-plate cases (black) flows.

Autocorrelations of v' in the $x-z$ plane in inner and outer regions are also compared between all cases in Figure 7. At $y/\delta = 0.1$, the correlations match well. However, at $y/\delta = 0.8$ the negative correlation contour in the outer region present in the results of Sillero et al. [9] is missing in both the flat-plate and airfoil boundary layers. This may be a Reynolds number effect.

The above comparison between the airfoil and flat-plate cases provides confidence that the inlet state of the flat-plate flow essentially matches with the airfoil boundary layer. This exercise also demonstrates that the boundary layer over the airfoil is fully turbulent at this location, after the laminar separation bubble at the leading edge and the subsequent transition to turbulence.

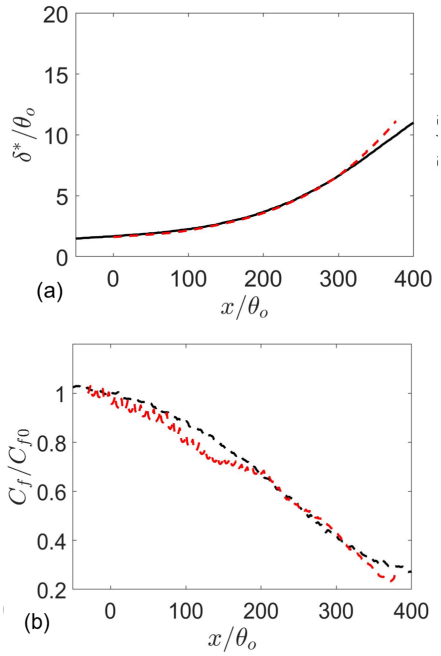

Figure 9: Comparisons of (a) displacement thickness and (b) skin friction coefficient (normalized by its value at x_0) between the airfoil (red) and flat-plate (black) cases.

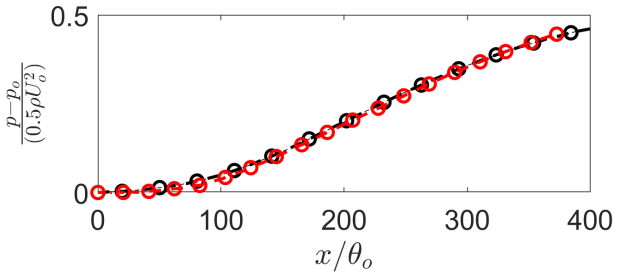

Figure 10: Wall pressure distribution comparison between airfoil (red) and flat plate (black). Here p_o and U_o are wall pressure and free stream velocity at x_o location.

3.2 Boundary layer development

To compare the developments of boundary layers between two cases, first the parameters representing the strength of effects of wall curvature (δ/R) and APG (β) are shown. Streamwise variation of boundary layer thickness in the case of airfoil with respect to its radius of curvature is shown in Figure 8(a). The higher δ/R near trailing edge indicates that curvature effects is strengthened along the streamwise direction. The Clauser parameter (Fig. 8(b)) shows an increase of value along x in both cases, suggesting that the strength of the pressure gradients relative to the near-wall forces increases with x. In addition, the β values are similar between the two cases throughout the most part of the boundary layer, except for a higher value in the airfoil case near the trailing edge, despite the matching $K(x)$ between the two cases; this is due to the lower wall friction in the airfoil case near the trailing edge as is shown next.

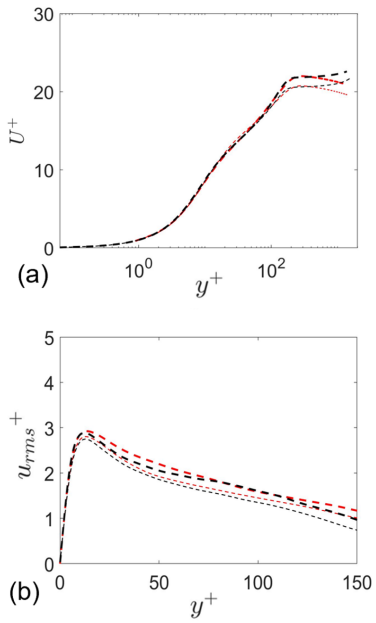

Figure 11: Comparison of (a) mean velocity profile and (b) streamwise velocity fluctuations (rms) normalized in inner units, between the airfoil (red) and flat plate (black) cases at x/θ_o =100 (thin dashed line) and 150 (thick dashed line).

Next, the boundary layer parameters are compared. First, the displacement thickness (δ^*) is compared in Figure 9(a). The overall variation matches well, except near the trailing edge where δ^* increases faster in the airfoil flow, which is probably a result of curvature effect due to the augmented β values along x. Figure 9(b) compares the skin friction coefficient (C_f), normalized by its respective values at the boundary layer inlet in both flows. The comparison shows a faster reduction in the skin friction in the airfoil flow for $x/\theta_0 <$ 150 (where $\beta < 1$, i.e. weak APG effect) and $x/\theta_0 > 290$

(where $\beta > 6$, stronger APG effect). In the weak-APG region ($x/\theta_0 < 150$), this lower C_f in the airfoil case is consistent with the effect of a convex curvature previously observed in ZPG flows or those with weak pressure gradients. The lower C_f near the trailing edge in the airfoil case explains the higher β in this region.

The wall pressure distribution are compared in Figure 10, which shows matching distributions between the two cases. The matching of mean wall pressure justifies the setup of the present DNS comparison; any difference in the boundary layer development between the two cases would be a result of the additional wall curvature effects in the airfoil case.

Figure 11 and 12 compare the y profiles of the streamwise mean velocity and turbulent statistics, at two different streamwise locations: $x/\theta_0 = 100$ and 150. At these x locations, the APG effects are weak as $\beta < 1$. It is shown that the velocity profiles overlap between the two cases. The streamwise fluctuations are slightly more intense for the airfoil flow; this may be a history effect of the upstream favorable pressure gradient in the airfoil case. The Reynolds shear stress (Figure 12b) $\langle\overline{u'v'}\rangle^+$ collapses near the wall between the two cases. But, away from the wall, $\langle\overline{u'v'}\rangle^+$ is lower in the airfoil case. Recall that $\langle\overline{u'v'}\rangle^+$ in the outer layer tends to be weakened by the wall curvature [3,4] and augmented by an APG [2,8]. The weaker outer-layer $\langle\overline{u'v'}\rangle^+$ suggests that, at these locations, the effect of curvature dominates that of APG. This is not surprising as the APG effect is weak at these x locations according to the local values of β.

At downstream locations of $x/\theta_o = 200$ and 250 as shown in Figure 13 and 14, where β ranges between 2 to 5, the velocity profiles and turbulent statistics appear to match between the two cases, which suggests that, although the curvature effect is strengthened as boundary layer thickened, the APG effect dominates that of the curvature.

Finally, two x locations near the trailing edge are compared in Figure 15 and 16, at $x/\theta_o = 300$ and 350. The APG is much stronger ($\beta > 7$) than upstream. At $x/\theta_o = 300$, the turbulent statistics match well between the flat-plate and airfoil flows. However, at $x/\theta_o = 350$, higher Reynolds stresses are observed for the airfoil flow far away from the wall, a feature of the APG effect. Recall that at $x/\theta_o = 350$ the β value is higher on the airfoil than on the flat plate (Figure 8(b)) due to the interaction between the effects of curvature and APG, the higher Reynolds stresses here suggest consistent domination of the APG effect over that of the curvature, as a result of such interaction.

The results above indicate that, in an airfoil boundary layer in the context of a fan flow, the convex wall curvature quantitatively modifies the boundary layer development. The effect of the curvature interacts with that of the APG by augmenting the strength of the pressure gradient perceived by the near-wall flow, which is characterized by β (a measure of the pressure gradient relative to the wall shear stress).

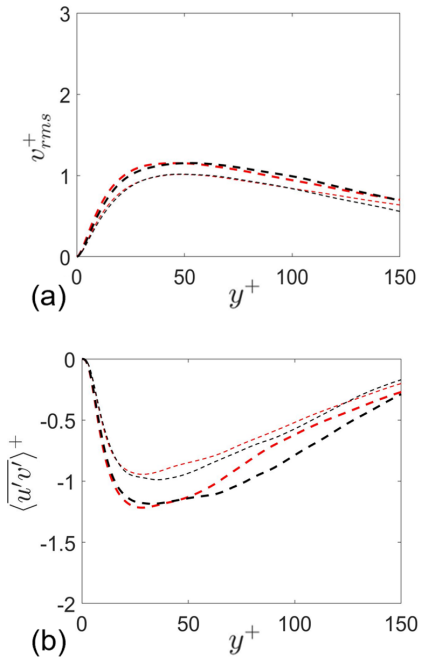

Figure 12: Comparison of (a) wall-normal velocity fluctuations (rms) and (b) Reynolds stress normalized in inner units, between the airfoil (red) and flat plate (black) cases at x/θ_o =100 (thin dashed line) and 150 (thick dashed line).

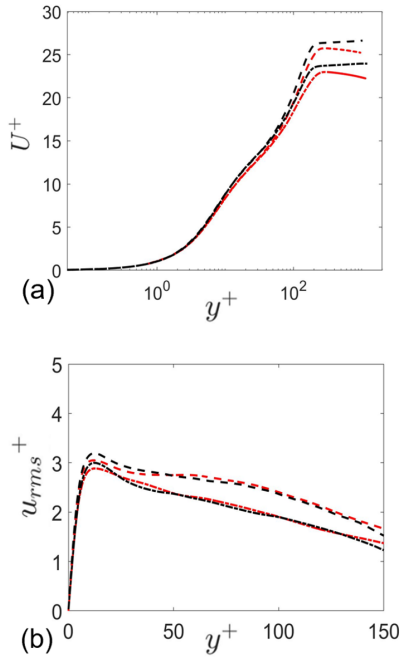

Figure 13: Comparison of (a) mean velocity profile and (b) streamwise velocity fluctuations (rms) normalized in inner units, between the airfoil (red) and flat plate (black) cases at $x/\theta_o = 200$ (dashed-dot line) and 250 (dashed line).

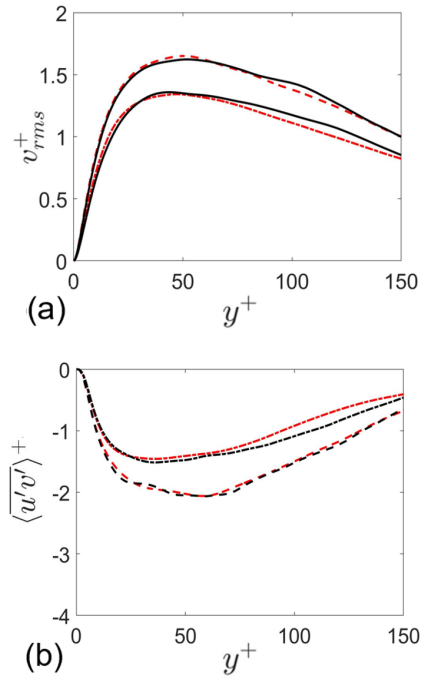

Figure 14: Comparison of (a) wall-normal velocity fluctuations (b) Reynolds stress normalized in inner units, between the airfoil (red) and flat plate (black) cases at $x/\theta_o = 200$ (dashed-dot line) and 250 (dashed line).

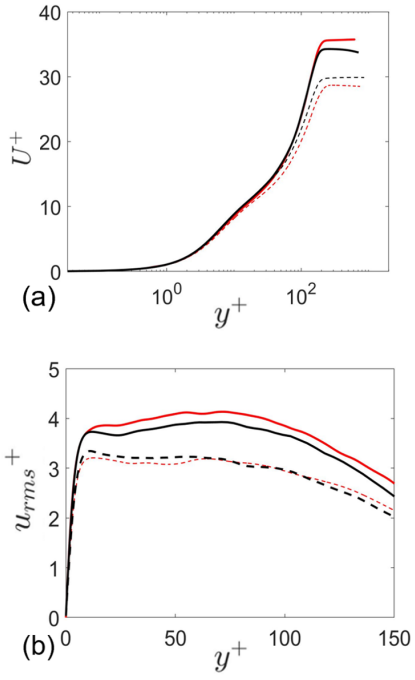

Figure 15: Comparison of (a) mean velocity profile and (b) streamwise velocity fluctuations (rms) normalized in inner units, between the airfoil (red) and flat plate (black) cases at $x/\theta_o = 300$ (dashed line) and 350 (solid line).

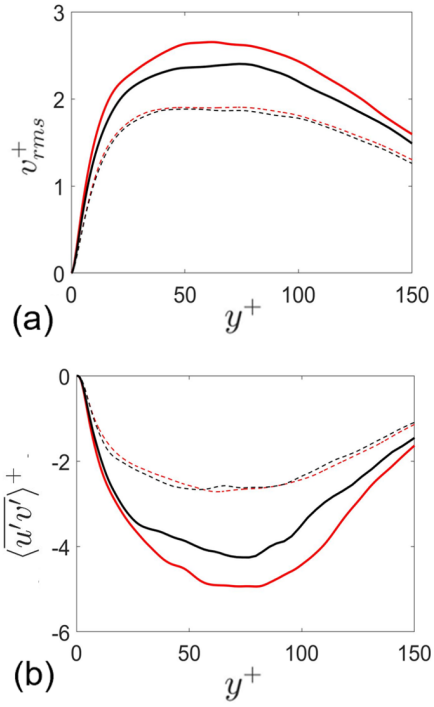

Figure 16: Comparison of (a) wall-normal velocity fluctuations and (b) Reynolds stress normalized in inner units, between the airfoil (red) and flat plate (black) cases at $x/\theta_o = 300$ (dashed line) and 350 (solid line).

4 Conclusion

This study characterizes the effect of wall curvature in the presence of adverse pressure gradients, in a setup designed to approximate typical flows around a fan blade with a CD airfoil. To this end, flow statistics are compared between two DNS simulations of flows over a flat plate and an airfoil with matching acceleration parameter, $K(x)$.

Results show that, as the boundary layer develops, the strengths of both pressure gradient (β) and wall curvature (δ/R) vary in the streamwise direction. Individual effects of APG and curvature on the Reynolds stress appear to be dominant at different x locations. Specifically, far from the trailing edge, when the pressure gradient is relatively weak, the Reynolds stresses is lower in the outer region for the airfoil, indicating that the curvature effect dominates. On the other hand, the stronger outer-layer Reynolds stresses in the airfoil case near the trailing edge suggests that the APG effect dominates that of the curvature.

Another important indication is that, for an APG boundary layer, a convex wall curvature quantitatively modifies the boundary layer development. The effect of the curvature interacts with that of the APG by augmenting the strength of the pressure gradient perceived by the near-wall flow.

REFERENCES

[1] Wu, H., Moreau, S. and Sandberg, R.D. . Effects of pressure gradient on the evolution of velocity-gradient tensor invariant dynamics on a controlled-diffusion aerofoil at $Re_c = 150000$. *Journal of Fluid Mechanics*, (868):584-610, 2019.

[2] Bobke, A., Vinuesa, R., *Örlü*, R. and Schlatter, P. History effects and near equilibrium in adverse-pressure-gradient turbulent boundary layers. *Journal of Fluid Mechanics*, 24(2), 820: 667-692, 2017.

[3] Bradshaw, P. The analogy between streamline curvature and buoyancy in turbulent shear flow. *Journal of Fluid Mechanics*, 36, no.1: 177-191, 1969.

[4] So, R.M. and Mellor, G.L. Experiment on convex curvature effects in turbulent boundary layers. *Journal of Fluid Mechanics*, 60(1), pp.43-62., 1973.

[5] Yuan, J. and Piomelli, U. Numerical simulation of a spatially developing accelerating boundary layer over roughness. *Journal of Fluid Mechanics*, 780, pp.192-214, 2015.

[6] Spalart, P.R.. Direct simulation of a turbulent boundary layer up to $R_\theta = 1410$. *Journal of Fluid Mechanics*, 187, pp.61-98, 1988.

[7] Schlatter, Philipp, and Ramis Örlü. Assessment of direct numerical simulation data of turbulent boundary layers. *Journal of Fluid Mechanics*, 659, pp.116-126, 2010.

[8] Na, Y., and Parviz Moin. Direct numerical simulation of a separated turbulent boundary layer. *Journal of Fluid Mechanics*, 374 (1998): 379-405.

[9] Sillero, J.A., Jimenez, J. and Moser, R.D. Two-point statistics for turbulent boundary layers and channels at Reynolds numbers up to $\delta+ \approx 2000$. *Physics of Fluids*, 105109 (2014): 1-30.

[10] Keating, A., Piomelli, U., Bremhorst, K. and Nesic, S. Large-eddy simulation of heat transfer downstream of a backward-facing step. *Journal of Turbulence*, 5(20) (2004), pp.1-3.